Lagrangian flow networks for passive dispersal: Tracers versus finite-size particles

Deoclécio Valente,[1] Ksenia Guseva,[2] and Ulrike Feudel[1,*]
[1]*Carl-von-Ossietzky Universität Oldenburg, D-26111 Oldenburg, Germany*
[2]*Centre for Microbiology and Ecosystem Science, University of Vienna, A-1090 Vienna, Austria*

(Received 16 March 2023; accepted 24 July 2024; published 27 August 2024)

The transport and distribution of organisms such as larvae, seeds, or litter in the ocean as well as particles in industrial flows is often approximated by a transport of tracer particles. We present a theoretical investigation to check the accuracy of this approximation by studying the transport of inertial particles between different islands embedded in an open hydrodynamic flow aiming at the construction of a Lagrangian flow network reflecting the connectivity between the islands. To this end, we formulate a two-dimensional kinematic flow field which allows the placement of an arbitrary number of islands at arbitrary locations in a flow of prescribed direction. To account for the mixing in the flow, we include a von Kármán vortex street in the wake of each island. We demonstrate that the transport probabilities of inertial particles making up the links of the Lagrangian flow network essentially depend on the properties of the particles, i.e., their Stokes number, the properties of the flow, and the geometry of the setup of the islands. We find a strong segregation between aerosols and bubbles. Upon comparing the mobility of inertial particles to that of tracers or neutrally buoyant particles, it becomes apparent that the tracer approximation may not always accurately predict the probability of movement. This can lead to inconsistent forecasts regarding the fate of marine organisms, seeds, litter, or particles in industrial flows.

DOI: 10.1103/PhysRevE.110.025103

I. INTRODUCTION

The dynamics of passive advection of small finite-size particles are ubiquitous to many processes within marine ecology and industrial systems. Precise predictions about the trajectories and final fate of these particles, representing organisms, seeds, waste, or plastic particles are crucial for understanding central phenomena in both settings. In marine systems, passive transport by ocean currents significantly impacts the dispersion of nutrients, pollutants, seeds, marine organisms, and marine aggregates. Models of this transport contribute to our understanding of ecological dynamics such as, e.g., the transport of harmful algal blooms [1], the connectivity of habitats [2,3], biogeochemical cycles [4,5], and the spread of contaminants in the marine environment [6,7]. Similarly, in industrial settings, passive transport is a key factor in the movement of particles within engineered systems, where the objective is to manipulate trajectories, for example, to achieve size-based segregation [8,9], to tune the outcome of mixing or aggregation-fragmentation processes [10,11], or even to guide targeted transport [12,13]. Moreover, for industrial applications, it is important to study the dependence of the rheological properties of the flow on the volume fraction of the particles and their density [14–16].

Of particular interest is the long-distance passive transport in marine environments. It ranges from the distribution of seeds of plants among islands and coastal areas [17–20] via the transport of larvae of different organisms between habitats [21–23] up to the fate of litter which is transported through the sea [24] or into the ocean from coastal areas [25]. This transport is determined by ocean flows possessing preferred directions which are influenced by prevailing wind directions and mesoscale hydrodynamic structures such as vortices, jets, and fronts [26–28]. One of the challenges is the identification of the major pathways of particles such as the pathways of micro- and macroplastics [29] and the locations where this litter concentrates in the ocean [30,31], the pathways of seeds to understand the distribution of plant species on different archipelagos in the world's ocean [32], or the pathways of larvae to get from spawning areas back to their reefs [33].

The simplest way to study this transport is to consider the particles as pointlike tracers neglecting their size and densities and use a Lagrangian approach for the transport of these particles [34–36]. In this case, the particle trajectories exactly follow the trajectories of the fluid parcels. To quantify the transport between different locations, it is sufficient to follow a large number of tracers from a release location to a target location and count the number of particles which reach the latter. This approach leads to Lagrangian flow networks which have been constructed for several regions in the world such as the Caribbean Islands [37] or connections between hydrodynamic provinces in the Mediterranean [2]. These studies are mostly based on ocean flows, while more theoretical approaches are based on kinematic flows [38–41]. We note that the use of the tracer approach, in general, offers very good predictions to the long-distance dispersal dynamics of particles in marine systems [42].

A more sophisticated approach is to approximate those particles as spheres with a certain size and density and treat them as inertial particles experiencing various forces in the flow. The trajectories of inertial particles in a given flow field can then be computed by solving the Maxey-Riley-Gatinol equation [43–45]. Those trajectories deviate notably from the ones of tracers leading to preferential concentrations [46–50], deviations in lateral transport [51], as well as sedimentation

*Contact author: ulrike.feudel@uol.de

[52–54]. The flow fields employed in works using this description range from simple two-dimensional kinematic flows mimicking, e.g., the flow in the wake of an island [27,55], to random and turbulent flows [47,56,57].

Motivated by the many aforementioned possible applications, we provide here a theoretical study in which we combine the idea of constructing Lagrangian flow networks, which has been so far restricted to tracer transport between release and target regions with the transport of inertial particles. Therefore, we use the Maxey-Riley equations to build up such Lagrangian flow networks for inertial particles and compare them with the ones obtained for tracers. We show that depending on the size and density of particles, those networks deviate from the ones realized by tracers. The most striking observation is that the tracer transport overestimates the probabilities for certain pathways, leading to flow network with many links, while the network obtained for particles with large Stokes numbers are much sparser. It has been demonstrated that particles having a density larger than the fluid (aerosols) are expelled from the vortices, while particles with a density lighter than the fluid (bubbles) are gathered within vortices [56,58]. These properties of inertial particles influence their paths and, hence, the development of Lagrangian flow networks. To systematically study the transport probabilities between different locations in the flow under the influence of mesoscale hydrodynamic vortices, we analytically construct a two-dimensional kinematic velocity field mimicking major properties of an ocean flow such as a preferred flow direction and the emergence of a von Kármán vortex street in the wake of islands. Our flow field allows for an arbitrary number of islands embedded in the flow in an arbitrary geometry. Those islands are considered as the release and target regions for the inertial particles. We quantify the differences in the connectivity, i.e., the probability of transport from one island to another, depending on the properties of the particles, such as size and density, and the properties of the flow, such as vortex strength and background velocity.

The paper is organized as follows. In Sec. II, we develop the velocity field which mimics the transport between n islands embedded in the flow and recall briefly the Maxey-Riley equations which are used to compute the transport of spherical inertial particles in this flow. Then, in Sec. III, we start with the characterization of the main differences in the advection dynamics between tracers and inertial particles. Next, we analyze the spatial distribution of the particles depending on the flow and particle properties and demonstrate the large heterogeneities in the locations to which particles are transported. Furthermore, we measure the connectivity between the different islands by computing the probabilities of transport between the islands and work out the substantial differences depending on the size and density in comparison to the usual tracer approach. Finally, we quantify the deviations in the transport probabilities when modeling inertial particles as pointlike tracers. We discuss the results in Sec. IV.

II. METHODS AND THEORETICAL BACKGROUND

A. The hydrodynamic flow

To study the connectivity among different islands embedded in a hydrodynamic flow in detail, it is useful to have an analytical two-dimensional (2D) flow field which allows for an arbitrary choice of the number of islands and their location in the flow. In this way, one can systematically change the geometry of the setup and the properties of the flow field. To achieve this goal, we extend a well-known kinematic flow to an arbitrary number of islands. The starting point is the flow field developed by Jung *et al.* [55], which considers one island embedded in the flow with a given flow direction in which the island acts as an obstacle, giving rise to a von Kármán vortex street in its wake. As an extension of this framework, we consider a two-dimensional kinematic flow with n embedded islands of circular shape with radius r_i $(i = 1, \ldots, n)$ and of the same size, $r_i = r \ \forall i$. The position of the islands is fixed according to an arbitrary, but prescribed geometry. We consider a two-dimensional observation area in which a main flow is assumed to flow from left to right along the x direction with different islands along is path. Far away from the position of the islands, in the y direction, the flow is expected to be uniform. Behind each island, a pair of counter-rotating vortices is created, at locations slightly below and above the center of the corresponding island, with a time difference of half a period, $T_c/2$. They move a distance L along the x direction during one period T_c, until they disappear due to dissipation. This process mimics the emergence of a von Kármán vortex street in the wake of each island. Since the flow under consideration is incompressible, a stream function $\varphi = \varphi(x, y, t)$ can be defined such that the two velocity components can be computed as derivatives of this stream function,

$$u_x = \frac{\partial \varphi}{\partial y}, \quad u_y = -\frac{\partial \varphi}{\partial x}. \tag{1}$$

The stream function for a velocity field with an arbitrary number of islands, say, n islands, at arbitrary positions $[(h_i, k_i),\ i = 1, \ldots, n]$ is given by

$$\varphi = \sum_{i=1}^{n} [f_i(x, y) g_i(x, y, t)] - u_0(n-1)y. \tag{2}$$

The terms from left to right are explained as follows: the first factor $f_i(x, y)$ ensures the presence of a boundary layer around each island such that the velocity field goes to zero at the boundary of each island,

$$f_i(x, y) = 1 - e^{-a_i\left(\sqrt{(x-h_i)^2+(y-k_i)^2}-r_i\right)^2}, \quad i = 1, \ldots, n, \tag{3}$$

where (h_i, k_i) are the spatial coordinates of the centers of each island i. The coefficient $1/\sqrt{a_i}$ mimics the width of the boundary layer. This assures that at the boundary of each island, the tangential velocity tends linearly to zero, while the radial velocity component decreases quadratically with the distance from the boundary.

The second factor $g_i(x, y, t)$ models the von Kármán vortex street and the main background flow u_0 reads

$$g_i(x, y, t) = \omega_{1i} H_{1i} g_{1i} + \omega_{2i} H_{2i} g_{2i} + u_0 y s_i(x, y), \quad i = 1, \ldots, n. \tag{4}$$

The first two terms in Eq. (4) describe the presence of the counter-rotating vortices in the wake of each island. These vortices are of equal strength, but opposite in sign, $\omega_{1i} = -\omega_{2i}$.

TABLE I. The representative parameters used in the model, unless specified otherwise, and their respective nondimensional values.

Parameter	Symbol	Dimensionless
Radius of the island	r_i	1
Period of the flow	T_c	1
Main background flow	u_0	12
Strength of the vortex	$\lvert\omega_{pi}\rvert$	40 or 60
Characteristic ratio	α_i	1
y coordinate of the vortex	y_{0i}	0.5
Travel distance of the vortices	L_i	4
Width of the boundary layer	a_i	1
Linear size of the vortices	R_{0i}	1

They are of Gaussian shape, formulated by the following function:

$$g_{pi}(x,y,t) = e^{-R_{0i}\{-[x-x_{pi}(t)]^2+\alpha_i^2[y-y_{pi}(t)]^2\}}, \quad p=1,2 \quad \text{and} \quad i=1,\ldots,n, \tag{5}$$

with $1/\sqrt{R_{0i}}$ and α_i being the radius and the characteristic ratio between the elongation of the vortices in the x and y direction, respectively. The strength of the vortices, ω_{pi} ($p=1,2$; $i=1,\ldots,n$), is modulated by

$$H_{1i}(t) = \sin^2(t\pi), \tag{6a}$$

$$H_{2i}(t) = \cos^2(t\pi). \tag{6b}$$

The centers of the vortices move, along the horizontal direction x, according to

$$x_{1i}(t) = h_i + r_i + \mathrm{L}_i \bmod (t, T_c), \tag{7a}$$

$$y_{1i}(t) = k_i + y_{0i}, \tag{7b}$$

$$x_{2i}(t) = x_{1i}(t - T_c/2), \tag{7c}$$

$$y_{2i}(t) = k_i - y_{0i}, \quad i=1,\ldots,n. \tag{7d}$$

The third term in Eq. (4) provides the contribution of the main background flow u_0. The factor

$$s_i(x,y) = 1 - e^{[-(x-h_i-r_i)^2/\alpha_i^2-(y-k_i)^2]}, \quad i=1,\ldots,n, \tag{8}$$

is the shielding factor associated with each island. This factor suppresses the impact of the background flow in the wake of the corresponding island. We display the nondimensional values of the parameters used in the model in Table I; a possible parametrization can be found in [40]. Note that Eq. (2) is an extension of the velocity field developed in [55] to an arbitrary number of islands at arbitrary positions. The presence of the last term in Eq. (2) is a direct consequence of the linear superposition principle assumed for the construction of the flow field. This term is necessary to assure that the main background flow u_0 is not counted as often as the number of islands. Furthermore, it is important to note that the linear superposition principle is only valid provided that the shielding areas, s_i, s_j, associated with two neighboring islands, respectively, do not overlap. This condition poses a restriction on the distance between neighboring islands, such that they cannot be placed too close to each other.

Nonetheless, one of the main advantages of our extended velocity field is the generality which allows for the study of an almost arbitrary location of the islands. This enables us to systematically vary the flow properties and the geometry of the arrangement of the islands to find out that the relationship between the properties of the particles and the flow determines the connectivity between the islands. We nondimensionalize the stream function given by Eq. (1) by measuring the length in terms of units of the radius of the island, r. As a unit of time, we take the period of the flow, T_c.

B. Advection of particles

The simplest approach to describe the motion of particles advected by fluid flows is to assume that these particles are just passive pointlike tracers that take on the same velocity as the surrounding fluid parcels. The velocity $\mathbf{V}$ of these pointlike tracer particles, or shortly *tracers*, is therefore the same as the velocity of the flow field $\mathbf{u}$ at the particle's position $\mathbf{X}$,

$$\dot{\mathbf{X}} = \mathbf{V}(\mathbf{X},t) = \mathbf{u}(\mathbf{X},t). \tag{9}$$

However, there are many cases where these above assumptions do not hold, and one has to consider that particles have a considerable size and density [59]. Such finite-size particles have a delayed reaction response to the flow dynamics. Their trajectories substantially deviate from the fluid parcels due to the action of several forces and, for this reason, they are also known as *inertial* particles in the literature. For spherical particles, these forces are described using the Maxey-Riley-Gatinol equations [43,44] with inclusion of a correction made by Auton [45]. In this work, we use a simplified version of these equations, neglecting the Faxén corrections [44] and the history force [11,27]. This approximation in its dimensionless form is given by

$$\dot{\mathbf{X}} = \mathbf{V}(\mathbf{X},t), \tag{10a}$$

$$\dot{\mathbf{V}} = \beta D_t \mathbf{u}(\mathbf{X},t) - \frac{1}{\mathrm{St}}[\mathbf{V}(\mathbf{X},t) - \mathbf{u}(\mathbf{X},t)], \tag{10b}$$

where $D_t = \partial_t + \mathbf{u}\cdot\nabla$ represents the derivative along the flow trajectory. The first term in this equation includes the added mass effect accounting for the necessary displacement of fluid by a moving particle and the acceleration of the fluid. The second term is the Stokes drag proportional to the difference between the velocities of the particle and the fluid. The two dimensionless parameters are $\beta = 3\rho_f/(\rho_f + 2\rho_p)$, the ratio between fluid ρ_f and particle ρ_p densities, and the Stokes number given by $\mathrm{St} = \frac{\alpha_p^2}{3\beta\nu\tau_f}$, where α_p is the size of the particle, ν is the kinematic viscosity, and τ_f is the characteristic flow time. If the particles are denser than the fluid, i.e., $\beta < 1$, they are known as aerosols; if they are lighter than the fluid, i.e., $\beta > 1$, we call them bubbles; and if $\beta \equiv 1$, they are known as neutrally buoyant particles. The density of the fluid (ρ_f) equals the density of water, approximated by the value $\rho_f = 1000\ \mathrm{kg/m^3}$. Note that Eq. (9) is valid as long as the particle Reynolds number is small, $\mathrm{Re}_p \ll 1$.

For our simulations, we choose two different Stokes numbers, which are $\mathrm{St} = 10^{-3}$ and $\mathrm{St} = 0.03$, and hold the following parameters fixed: $\beta = 0.495$ for aerosols, $\beta = 1.875$ for bubbles, and $\beta = 1$ for neutrally buoyant particles.

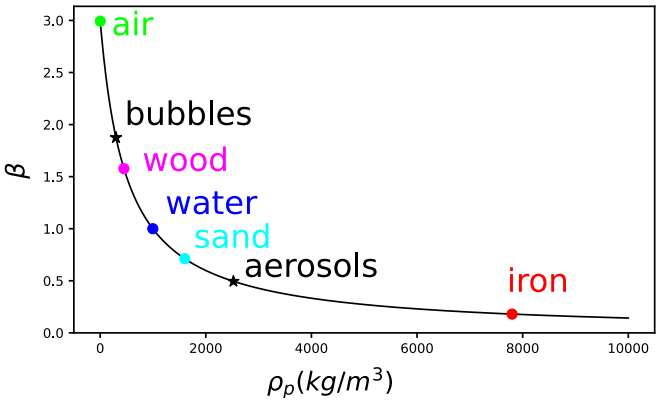

FIG. 1. Comparative analysis of finite-size particle properties based on density and relative size. This graph plots various particles, including air, bubbles in our simulations, wood, water, sand, aerosols in our simulations, and iron, showcasing the diversity in density (ρ_p) and dimensionless parameter β. The density of the fluid (ρ_f) which enters the parameter β corresponds to the density of water, approximated by the value $\rho_f = 1000\ \mathrm{kg/m^3}$.

Figure 1 illustrates that the chosen β values lie in a realistic range. However, those values as well as the selected Stokes numbers are quite far away from the Stokes numbers of real seeds or organisms in an ocean flow. According to our aim to provide a theoretical study, we made a choice which better illustrates the impact of inertia.

C. The geometric setup for particle transport

To study the transport of particles in a general framework of an arbitrary number of islands embedded in a flow, we employ two different geometrical setups composed of six islands each. One of them is a chain of islands (COI), where all islands are arranged in a chain similar to the setup in [56,60]. The other one is a random geometry (RG), with randomly chosen positions of the islands. While in the COI, the islands are equally spaced, in the RG, they are not (see Fig. 2). The main flow in both setups is directed along the x axis from left to right.

We fix four different locations as sources of particles S_i with $i = 0, 1, 2, 3$, at which we release particles. One of these locations is upstream at the line $(x = -5, y \in [-3, 3])$ and $(x = -5, y \in [-5, 5])$ for COI and RG, respectively, from where particles advected by the main background flow u_0 enter the observation area at $x = -5$. The other three locations are in a ring of width 0.4 around each of the first three islands, respectively, representing other locations from where particles start (see Fig. 2). In addition, we fix seven target locations O_j with $j = 1, \ldots, 7$, which we check for particle visits. Six of these locations are in a ring of width 0.4 around each one of the islands. The other location is downstream of the observation area at $(x = 55, y \in [-3, 3])$ and $(x = 45, y \in [-5, 5])$ for COI and RG, respectively. For our particle advection experiments, we start with 150 particles in each S_i, $i = 0, \ldots, 3$, whose initial positions (x, y) are randomly chosen within the specified areas. The particles enter the system with the same velocity as the fluid particles at their release position. During each flow period, particles are released at a randomly selected time, denoted as τ, which is uniformly distributed. On average, approximately 10 000 particles are released per period. After being released, they are advected by the flow until they reach either one of the other target regions O_j, with $j = 1, 2, 3, 4, 5, 6$, or they escape at O_7, which is the "end of observation area" (EOA) located at the right boundary at $x = 55$ (COI) and $x = 45$ (RG), respectively. Importantly, we only consider that the particle has reached the given target when this particle has crossed the boundary of this region (the ring of width 0.4 around each island). Once inside the ring, few particles can get very close to the island and would stay there for an extremely long time since the flow velocity goes to zero

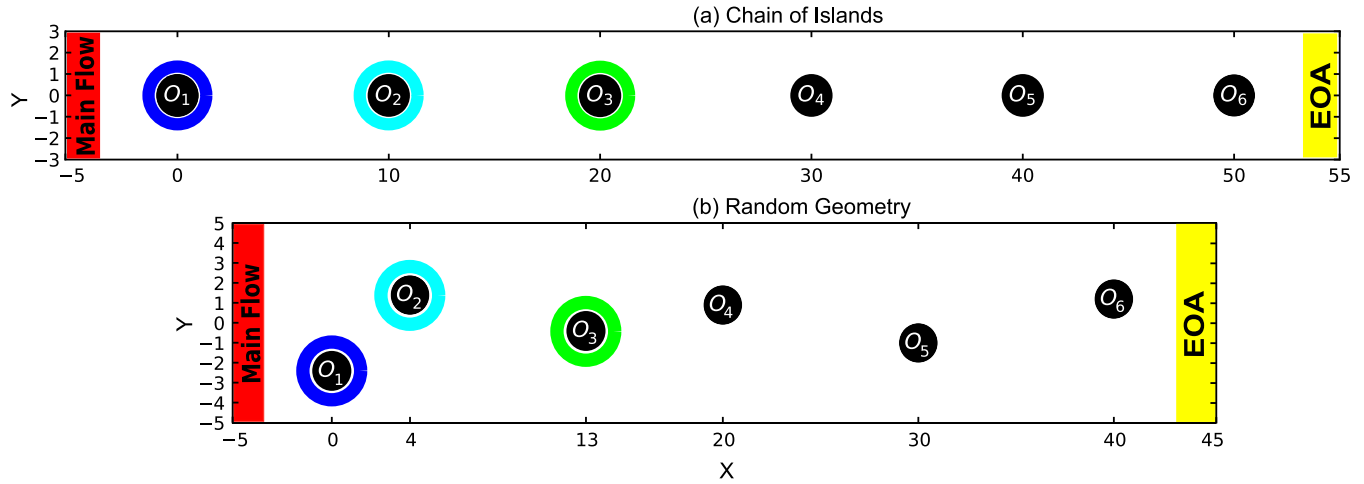

FIG. 2. Two geometrical setups are considered: (a) chain of islands (COI) and (b) random geometry (RG). For both geometries, we schematically represent the release area of particles at the start of the observation area S_0 [shown as a dark strip (red) at $x = -5$], and three additional sources around each one of the first islands: S_1 (dark blue ring around O1), S_2 (cyan ring around O2) and S_3 (green ring around O3). We also show the target region at the end on the observation area at $x = 45$ marked as EOA in yellow. In addition (not shown), all of the islands have a target region around them; they are equivalent to the source regions described above for the first three islands.

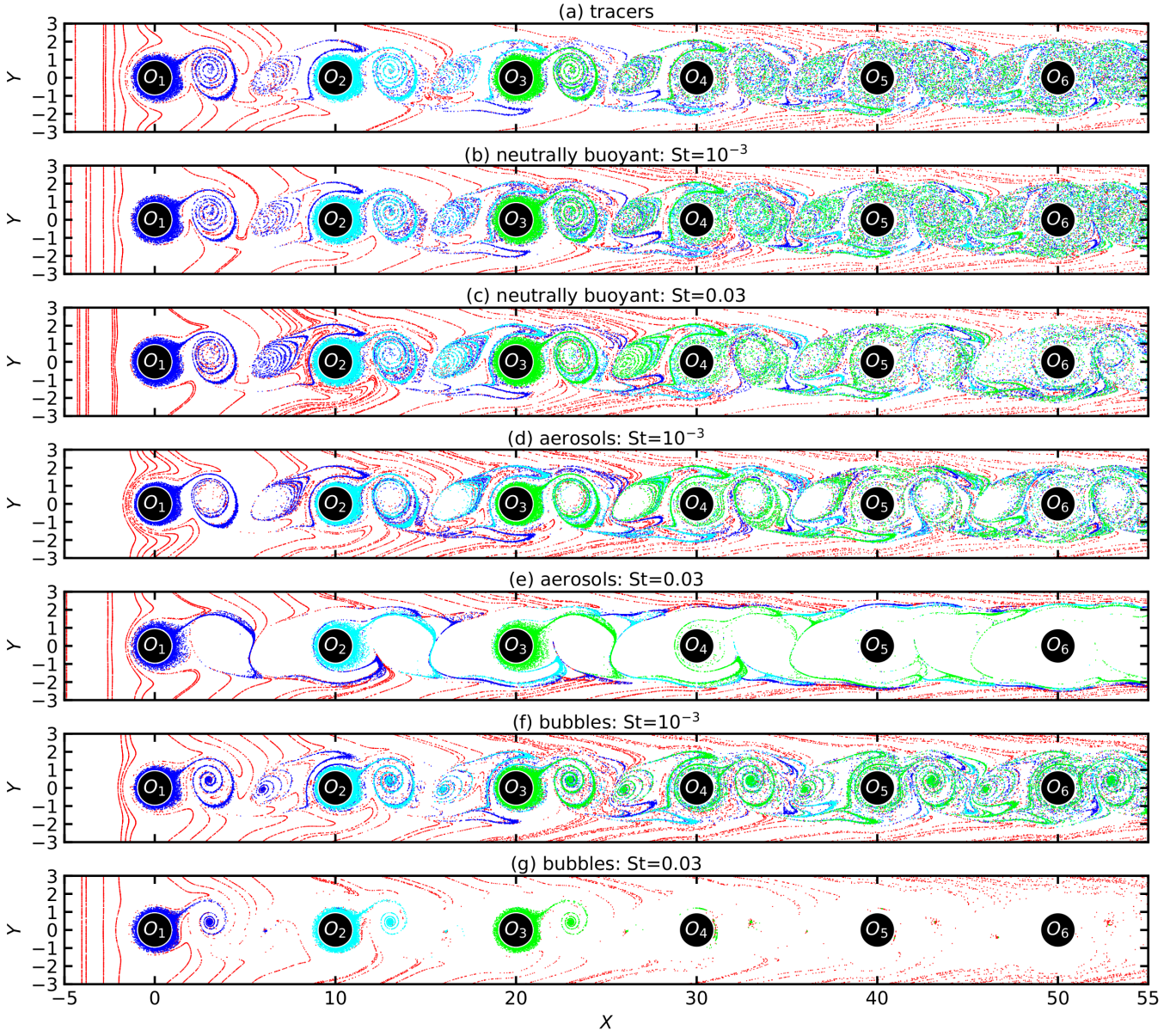

FIG. 3. Spatial distribution of tracers and inertial particles in the wake of six islands. From the top to the bottom: (a) ideal tracers; (b),(c) neutrally buoyant particles for St $= 10^{-3}$ and St $= 0.03$, respectively; (d),(e) aerosols for St $= 10^{-3}$ and St $= 0.03$, respectively; and (f),(g) bubbles for St $= 10^{-3}$ and St $= 0.03$, respectively. Those snapshots were taken at a time $23.48T_c$ for vortex strength $\omega = 60$. Colors correspond to the colors in Fig. 2.

at the boundary of the island. We check for those particles with another ring of width 0.014 around each island. All particles which enter this very small ring are removed. Although their number is small, we still subtract it from the total number of released particles and we discard them from further statistics. In the y direction, the boundaries of the observation area are open. With this setup, we are able to count how many particles are advected from each of the source regions S_i $(i = 0, \ldots, 3)$ to each of the target regions O_j $(j = 1, \ldots, 7)$. Measuring the time interval from release to reaching one of the targets allows us to determine the time needed to be advected from one location to another. Since many particles visit different islands on their way from the source to the end of the observation area, we can follow their whole path in the flow.

III. RESULTS

A. Comparing trajectories of inertial particles with tracers

General aspects of advection dynamics

We start our analysis by characterizing the main differences in the advection dynamics of our four types of particles (tracers, neutrally buoyant particles, bubbles, and aerosols). As described in the methods, we have a continuous influx of particles from four source areas and the escape of these particles at the right boundary of the observation area (see Fig. 2). After a short transient, the picture becomes periodic due to the periodic flow. From this time on, the ensemble of the injected particles spreads through the whole observation area, forming dynamic fractal patterns, which strongly vary for the four par-

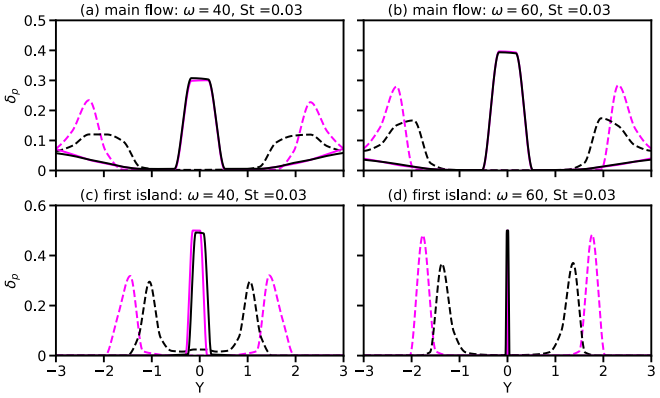

FIG. 4. The distribution of aerosols and bubbles along the y axis after crossing half of the observation area at $x = 25$ (black lines) and the whole observation area at $x = 55$ (magenta lines). Particles were released within the setup with a chain of islands (COI) in the observation area with dimensions $[-5, 55]\times[-3, 3]$. The line styles represent the particles: aerosols (dashed lines) and bubbles (solid lines). The different rows identify the source locations: (a),(b) main flow (S_0) and (c),(d) first island (S_1). We only show the results for the large Stokes number $\mathrm{St} = 0.03$.

ticle types. We illustrate these patterns by taking a snapshot of the spatial distribution of particles at $t = 23.48T_c$ (see Fig. 3) and we compare the different particle types. We can see that while the differences to tracers are more subtle for $\mathrm{St} = 10^{-3}$, they are very pronounced for large $\mathrm{St} = 0.03$. As expected, the strongest similarity can be observed in the spatial distribution of tracers and neutrally buoyant particles. We also observe the well-known trapping of bubbles in the vortices and the ejection of aerosols from the vortices in the flow field [56]. These effects are already present at $\mathrm{St} = 10^{-3}$ and especially visible for $\mathrm{St} = 0.03$ (see Fig. 3). These differences in the advection of tracers and inertial particles should clearly translate into contrasting transport properties for different particle types.

Before we quantify the transport between the different locations, we study the distribution of aerosols and bubbles along the observation area depending on the strength of the vortices, the geometrical setup with respect to the position of the islands, and the place where the particles are released.

To this end, we have fixed two lines along the y axis, i.e., one in the middle of the observation area ($x = 25$) and the other at the end ($x = 55$). We were interested in registering the y coordinates of all particles to create spatial distributions when the particle crosses the middle and the end of the observation area. We show the results for COI geometry, which is easier to interpret due to its symmetry, for two vortex strengths ($\omega = 40$ and $\omega = 60$) and different release sources (i.e., main flow and first island). To make the distributions along those lines comparable, we normalize each of them by the total number of particles crossing the corresponding line. In Fig. 4, we represent the normalized distributions δ_p, which show the proportion of particles crossing the lines $x = 25$ and $x = 55$ during a simulation time. In what follows, we will only show and discuss the distribution for the most extreme case of aerosols and bubbles. Since inertial effects are larger for large Stokes numbers, we consider only $\mathrm{St} = 0.03$; for $\mathrm{St} = 10^{-3}$ the influence of inertia is less pronounced.

The results quantify the observations already presented in Figs. 3(d) and 3(e). Due to the centrifugal forces which aerosols experience in the vortices, they move further away from the symmetry axis at $y = 0$. This behavior is observed for particles released with the main flow [dashed line in Figs. 4(a) and 4(b)] as well as the ones released at the first island [dashed line in Figs. 4(c) and 4(d)]. With increasing distance from the release location, the maximum concentration of particles moves away from the symmetry axis as expected [compare the black ($x = 25$) and magenta ($x = 55$) curves]. Increasing the vortex strength from $\omega = 40$ (Fig. 4, left panels) to $\omega = 60$ (Fig. 4, right panels) intensifies the centrifugal forces and leads again to a further movement away from the symmetry axis.

By contrast, bubbles are trapped in the vortices, as already illustrated in Figs. 3(f) and 3(g). Therefore, the maximum of their concentration (solid line, Fig. 4) is around the symmetry axis because the location of the two vortex centers are at $y = -0.5$ and $y = 0.5$. Next to the maximum, we find a region of almost zero particles since those released with the main flow are also trapped. Due to the trapping phenomena, the maximum from $x = 25$ to $x = 55$ does not change. In addition, we find a nonzero distribution function δ_p in regions far away from the symmetry axis [Figs. 4(a) and 4(b)] as it corresponds to the particles transported with the main flow unaffected by the vortices. These parts of δ_p are, of course, absent for particles released at the first island.

Overall, we observe a clear segregation of aerosols and bubbles. While aerosols move away from the symmetry axis due to centrifugal forces, bubbles approach it. The larger the vortex strength, the stronger is the segregation. Other geometries break this symmetry and lead to a more mixed distribution of aerosols and bubbles.

B. Measuring connectivity between islands

In this section, we study the connectivity between islands by measuring the probability of transport of particles between source and target regions. To this end, we use the setups described in Sec. II C and introduce a probability measure to evaluate the transport between a source S_j and a target O_i by computing the probability P_{ij} as the ratio of the total number of particles transported from S_j to O_i and the total number of particles, N_j, released at S_j:

$$P_{ij} \approx \frac{\mathrm{Prob}\{S_j \rightarrow O_i\}}{N_j}. \tag{11}$$

This probability measure crucially depends on the physical properties of the particles, such as their Stokes number, as well as on the properties of the hydrodynamic flow, such as the background velocity u_0 and the strength of the vortices. Note that the probability to reach a location depends on the geometry of the setup, i.e., the positions of the islands in the flow. Although the choice of the target ring area influences the quantitative aspects, it does not affect the qualitative differences between the particle types. Once the transport between S_j and O_i has been quantified for all j and i, we can represent the connectivity as a weighted directed graph in which the nodes are given by the islands as source and target regions. We add the main flow (left boundary of the observation in

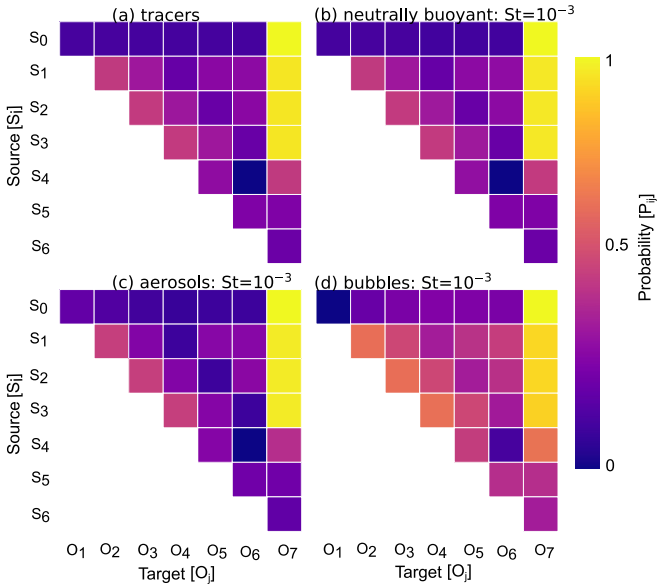

FIG. 5. The transport probabilities for tracers and inertial particles. Geometry: COI. Observation area $[-5, 55]\times[-3, 3]$. (a) Tracers, (b) neutrally buoyant particles, (c) aerosols, and (d) bubbles. Vortex strength $\omega = 40$.

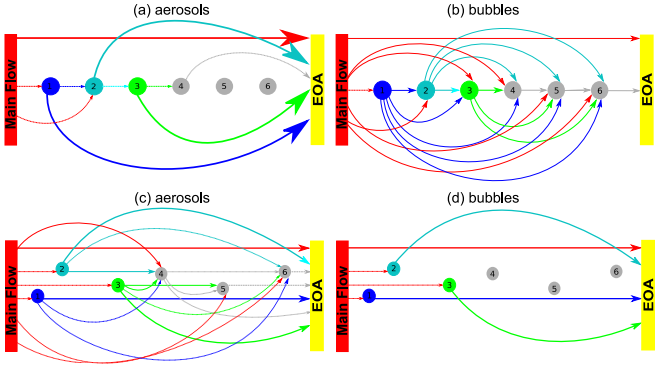

FIG. 6. Connectivity for different geometrical setups for the position of the islands. (a),(b) COI and observation area $[-5, 55]\times[-3, 3]$. (c),(d) RG and observation area $[-5, 45]\times[-5, 5]$. In (a) and (c), we display the connectivity for aerosols. In (b) and (d), we display the connectivity for bubbles. The vortex strengths and the Stokes number are $\omega = 40$ and $\mathrm{St} = 0.03$, respectively.

Fig. 2) as an additional source and the end of the observation area (right boundary of the observation area) as an additional target region. The edges of the graph are given by the transport probabilities; thereby, we only establish a link if the transport probability is larger than 0.01. This procedure constructs a Lagrangian flow network serving as a representation of the connectivity between different locations in a hydrodynamic flow. The matrix of probabilities P_{ij} contains the strength of the connections as weights that are multiplied with the adjacency matrix in graph theory, which usually contains only ones and zeros depending on whether or not a connection exists.

We now investigate how the strength of the links depends on the properties of the particles and the geometry. The differences in the spatial particle distribution in the flow depending on the Stokes number already revealed an important impact of the vortices (see Fig. 3 in Sec. III A) since we observed, as expected, that aerosols are expelled from vortices, while bubbles are attracted by them.

Let us first discuss the probability of the transport for the four particle types. Though we expect the largest impact for larger Stokes numbers, we choose to first discuss the smaller Stokes number $\mathrm{St} = 10^{-3}$ since we can show that even for small Stokes numbers where inertial effects are small, there is a considerable impact. Figure 5 shows the entries in the probability matrix, color coded by their strength. As expected, there are large similarities for tracers and neutrally buoyant particles, which are also reflected in the transport probabilities. Their values are close, but not equal, as shown in Fig. 5 where we present the matrix of transport probabilities in a logarithmic scale to emphasize smaller differences. More striking are the differences for aerosols and bubbles, as inertial effects play a bigger role. However, it is rather surprising that even for the case of such small Stokes numbers, where the impact of inertia is still quite small, the transport is different.

For the larger Stokes number, those differences in transport probabilities are much more pronounced and strongly depend on the geometry of the islands' positions. For illustration, we plot the graphs of connectivity for the two geometries (see Fig. 6). To visualize the Lagrangian flow network, we use the following convention for the strength of the connections: If the transport probability $P_{ij} < 0.01$, we do not draw any link; for $0.01 \leqslant P_{ij} < 0.1$, the connectivity is weak and drawn by a thin line; for $0.1 \leqslant P_{ij} < 0.5$, the connectivity is moderate, reflected by a medium size line; and, finally, for $0.5 \leqslant P_{ij} \leqslant 1$, the strong connectivity is visualized by a thick line. Using this classification, the results for vortex strength of $\omega = 40$ are shown in Fig. 6 for aerosols [Figs. 6(a) and 6(c)] and bubbles [Figs. 6(b) and 6(d)], respectively. We find that the impact of the geometry is quite different for aerosols and for bubbles. For aerosols [Figs. 6(a) and 6(b)], we observe relatively sparse connectivity compared to RG in the case of COI. This is due to the fact that aerosols are expelled from the vortices and this already happens mostly in the first von Kármán vortex street, which the particles enter after their release. As a consequence, they are expelled from the whole region where the islands together with the vortex streets are located along the x axis and move further outside this region without hitting any other island's influence until they reach the end of the observation area. This effect is even more pronounced for the stronger vortex strength (not shown). By contrast, in the RG geometry, there is no confined area in which the von Kármán vortex street is located and a particle can experience different islands and the vortices in their wake on their way through the observation area. Therefore, the connectivity is much larger with different probabilities connecting the different islands.

For bubbles [Figs. 6(b) and 6(d)], the situation is exactly opposite. Here a large connectivity is observed for the COI, but only a sparse one for RG. Since bubbles are entrained and transported by the vortices until the vortex disappears, they are moving inside the vortices from island to island in the chain leading to a large connectivity. By contrast, in RG, they will

also be entrained by a vortex, but when the vortex disappears due to dissipation, then they will be transported mainly by the background flow to the end of the observation area and only be influenced by other vortices if the geometry of islands permits the impact of another vortex. Since the impact of vortices decays exponentially with distance, such an influence is rather unlikely if the distance between islands is large enough.

Those results underline the paramount importance of the geometry of the islands' locations when inertial particles are considered and compared to tracers. While tracers and neutrally buoyant particles exhibit a large connectivity for all considered vortex strengths and geometries, this is not the case for inertial particles with larger Stokes numbers. In certain geometries, some locations can be reached only by one type of inertial particle (e.g., aerosols), but not by the other (e.g., bubbles). This fact leads to a separation of different types of particles in terms of transport. We observed high connectivity between islands only for the chain geometry COI for bubbles and for the random geometry RG for aerosols, while the connections for bubbles in RG and aerosols in COI are rather sparse. It is important to emphasize that in the case of low connectivity, we observe a number of islands which are not reachable at all. This is fundamentally different from the tracer and neutrally buoyant particle approach where all islands can be reached.

C. Estimation of the error in forecasting particle transport

In the previous section, we have shown that certain types of particles (aerosols and bubbles) cannot reach some islands in the flow, which tracers would do. However, many applications studying the spatial distributions of larvae, seeds, and litter such as plastic particles in the ocean use tracer models. The same applies to particle-laden flows in industrial settings, where the Stokes numbers could be larger. Usually, the argument is that the Stokes numbers of these objects are small to justify this approach. But there is no study as to what extent this argument is really valid. In this section, we quantify the deviations caused by approximating inertial particles by tracers. These deviations will be given by the factors λ_{ij} computed from the ratio of transport probabilities P_{ij} (see Sec. III B) for inertial particles and tracers: $\lambda_{ij} = \frac{P_{ij}^{\text{inertial}}}{P_{ij}^{\text{tracer}}}$. In such a case, λ_{ij} will describe how much the probability of transport of particles between source and target regions of inertial particles deviates from those computed for tracers. Since P_{ij}^{inertial} (see Sec. III B) is sensitive to the strength of the vortices (i.e., ω), the geometry (i.e., COI and RG), and the source of the particles (i.e., S_j), all these factors are reflected in λ_{ij}. Once λ_{ij} has been computed, we say that P_{ij}^{inertial} will be overestimated by the tracer approach (i.e., P_{ij}^{tracer}) if $\lambda_{ij} < 1$ and underestimated if $\lambda_{ij} > 1$. In the following, we compute the ratio of λ_{ij} for aerosols $\lambda_{ij}^{\text{a}} = \frac{P_{ij}^{\text{a}}}{P_{ij}^{\text{t}}}$ and bubbles $\lambda_{ij}^{\text{b}} = \frac{P_{ij}^{\text{b}}}{P_{ij}^{\text{t}}}$ with respect to tracers for both $\text{St} = 10^{-3}$ and $\text{St} = 0.03$, applying the vortex strength $\omega = 60$. Let us first discuss the situation for the chain geometry COI (Fig. 7) since there we have a systematic deviation due to symmetry of the setup. For aerosols [Figs. 7(a) and 7(b)], we find an overestimation of the transport modeled by tracers, while transport is systematically

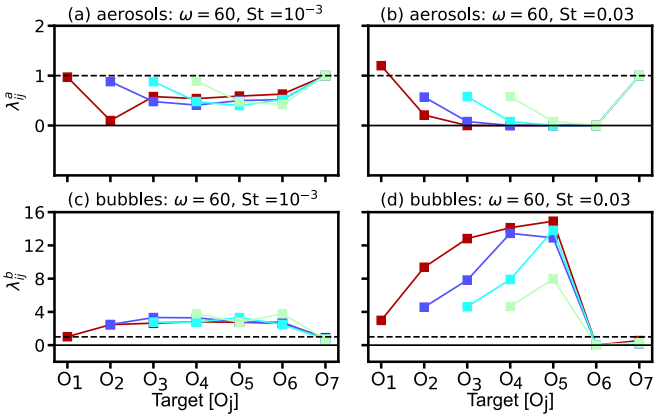

FIG. 7. The deviation of the transport probabilities between source and target regions for aerosols and bubbles in relation to tracers. Geometry: COI. Observation area $[-5, 55]\times[-3, 3]$. The dashed and solid black lines represent $\lambda_{ij}^{\text{t}} = 1$ and $\lambda_{ij}^{\text{t}} = 0$, respectively. The different colors help to identify the source location: S_0 (main flow) in red, S_1 (island 1) in blue, S_2 (island 2) in cyan, and S_3 (island 3) in green. We represent aerosols in (a) and (b), while (c) and (d) show results for bubbles.

underestimated for bubbles [Figs. 7(c) and 7(d)]. Even if the Stokes number is small, such as $\text{St} = 10^{-3}$, the deviation is considerable, namely, the transport of aerosols is only half of that modeled by tracers, and for bubbles, it is twice as large as the tracer equivalent. For the large Stokes number $\text{St} = 0.03$, the error is, as expected, much larger: aerosols in many cases do not even reach the targets and their transport becomes zero, while for bubbles the transport is up to 15 times larger than estimated by tracers. For the random geometry RG with its random island disposition, we do not find such large systematic deviations. Over- and underestimation of transport in this geometry strongly depends on the considered source and target locations. Particularly for bubbles, we observe that the transport probabilities approach zero even for the small Stokes number. For certain target locations, the transport probabilities would be larger by factors of 2 for aerosols or 5 for bubbles, even for the small Stokes number $\text{St} = 10^{-3}$. For the large Stokes number $\text{St} = 0.03$, the effects are much more pronounced, leading to factors of 5 for aerosols and of >12 for bubbles.

From those findings, we can conclude that one has to be very careful with predictions of studies of transport of particles based on tracers; the real objects should be treated as inertial particles to obtain reasonable estimates of particle transport.

IV. CONCLUSIONS

We have employed the Maxey-Riley-Gatinol equations to describe the motion of spherical inertial particles in a flow to establish the links in a Lagrangian flow network connecting a certain number of islands. In order to study such networks depending on the properties of the flow and the particles, we have introduced a kinematic two-dimensional flow field which allows for placing an arbitrary number of islands at prescribed positions in an open background flow with a given

direction. Using this approach, we have demonstrated that the Lagrangian flow networks for inertial particles may deviate quite substantially from the ones of tracer particles. As it is well known that inertial particles do not follow the flow exactly but have their own paths depending on their size and density, deviation from Lagrangian networks obtained with tracers had to be expected. Mesoscale hydrodynamic vortices in the flow cause segregation of aerosols and bubbles. Bubbles are entrained and transported within the vortex and released from it when the vortex disappears due to dissipation. By contrast, aerosols are expelled from vortices. As a consequence, some target regions can only be reached by bubbles and not by aerosols, and vice versa, depending on the geometry of the setup. Tracers and neutrally buoyant particles spread through the flow field and reach all parts of the observation area in slightly higher or slightly lower concentrations. Inertial particles, on the other hand, experience a much stronger effect of the vortices and concentrate only in certain regions of the flow field. The consequence is that they, in general, have a smaller probability to reach a target region; however, if they reached it, they would do it in much higher numbers. This is the reason why in a random geometry the connectivity is larger for aerosols and sparse for bubbles because the latter get trapped in the vortices. The opposite is true for the chain of island where we find higher connectivity for bubbles. These distinct connectivity pattern cannot be observed for tracers and neutrally buoyant particles, which in our setups always realized all possible connections. We can conclude that the computation of transport paths of inertial particles employing an approximation by tracers can lead to considerable over- or underestimation of transport probabilities.

According to our aim to provide a theoretical study of the impact of inertia on Lagrangian flow network, we have chosen Stokes numbers St and density ratios β which are rather different from seeds, larvae, or plastic particles in order to make the difference obvious. However, we could show that even for small Stokes numbers, the deviations are not negligible. Therefore, one should carefully check whether a tracer approximation is suitable if one wants to predict transport probabilities. In our study, we have restricted ourselves to two-dimensional flows, which neglects the possible sinking of particles having densities larger than the fluid. For such aerosols, the sinking process should also be taken into account. This also applies for the density ratio β, which we used for our study. But our focus was also on the impact of the geometry of the setup and this could only be achieved by using 2D flow, which is governed by a stream function. Therefore, we could not take sinking velocities into account.

Finally, we would like to address another simplification we made: The generation of the vortices was uniform across all islands such that they were synchronized in their behavior. In an additional study (see the Appendix), we have taken randomized times at which vortices detach from each island, which makes the setup more realistic. We find that as we would expect, more mixing is introduced in the flow field and particle distributions for small Stokes numbers look more similar to the ones of tracers and neutrally buoyant particles (see the Appendix, Fig. 8). However, qualitatively, we obtain the same results but with higher transition probabilities (Fig. 9) due to the increasing mixing and slightly different connectivity maps (Fig. 10).

ACKNOWLEDGMENTS

We want to thank Tamás Tél for the hospitality at Eötvös Loránd University Budapest, Hungary, which led to valuable discussions as well as suggestions. Furthermore, we would like to acknowledge the contributions of Bernd Blasius, Dirk C. Albach, Matthias Schroeder, Michael Kleyer, Rahel Vortmeyer-Kley, and, above all, the DFG research unit DynaCom. Finally, we acknowledge the HPC Cluster CARL with which the simulations were performed. It is located at the University of Oldenburg (Germany) and funded by the DFG through its Major Research Instrumentation Program (Grant No. INST 184/157-1 FUGG) and the Ministry of Science and Culture (MWK) of the Lower Saxony State, Germany. The authors acknowledge financial support from the Deutsche Forschungsgemeinschaft (DFG) for the Project No. 379417748, as subproject 6, "Modeling hydrodynamics and passive dispersal," in the research group DynaCom (Spatial community ecology in highly dynamic landscapes From island biogeography to metaecosystems, DFG/FOR 2716).

APPENDIX: DETAILED ANALYSIS OF RANDOMIZED VORTEX RELEASE

To reproduce the results here in the Appendix, we had to adjust the equations which describe the presence of the counter-rotating vortices in the wake of each island as follows:

$$g_{pi}(x,y,t) = e^{-R_{0i}\{-[x-x_{pi}(t)]^2+\alpha_i^2[y-y_{pi}(t)]^2\}}, \quad p=1,2 \quad \text{and} \quad i=1,\ldots,n, \tag{A1}$$

with $1/\sqrt{R_{0i}}$ and α_i as the radius and the characteristic ratio between the elongation of the vortices in the x and y direction, respectively. Here each pair of vortices moves a distance L during time T_c and then disappears due to dissipation. But the centers of the vortices are modulated by

$$H_{1i}(t+\delta_{ti}) = \sin^2[(t+\delta_{ti})\pi], \tag{A2a}$$

$$H_{2i}(t+\delta_{ti}) = \cos^2[(t+\delta_{ti})\pi], \tag{A2b}$$

which move along the horizontal direction x according to

$$x_{1i}(t+\delta_{ti}) = h_i + r_i + \mathrm{L}_i \bmod [(t+\delta_{ti}), T_c], \tag{A3a}$$

$$y_{1i}(t+\delta_{ti}) = k_i + y_{0i}, \tag{A3b}$$

$$x_{2i}(t+\delta_{ti}) = x_{1i}[(t+\delta_{ti}) - T_c/2], \tag{A3c}$$

$$y_{2i}(t+\delta_{ti}) = k_i - y_{0i}, \ i=1,\ldots,n. \tag{A3d}$$

Here the amplitude modulation and horizontal progression of vortices are governed by harmonic functions, with a temporal adjustment factor δ_{ti} reflecting the staggered release of vortices. The new component δ_{ti} introduces variability in the vortices' initiation. In the case of synchronization, all δ_{ti} values are set to zero for all vortices, which leads all of them to be released at the same time instant (the setup of the simulation described in the main text).

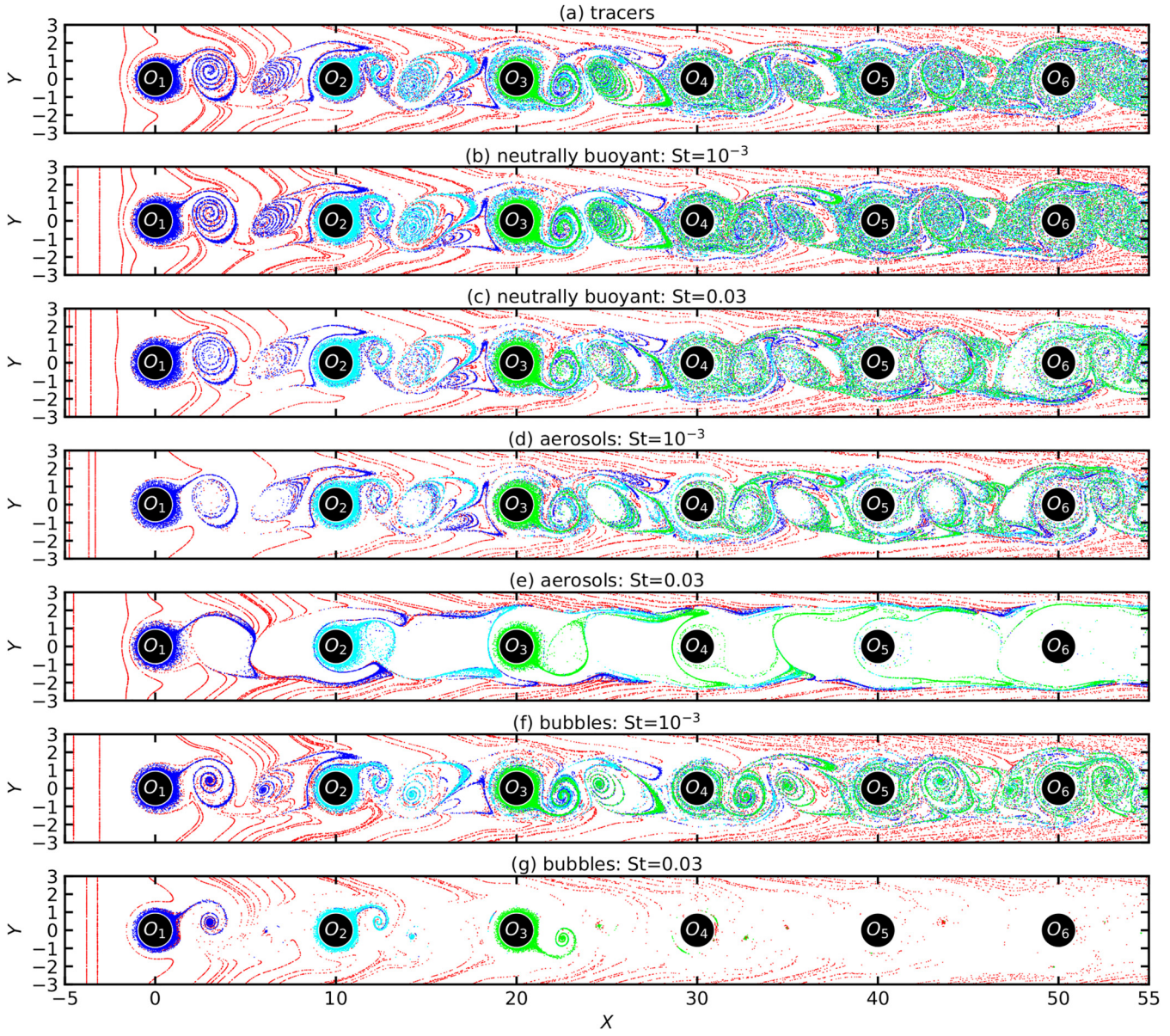

FIG. 8. Spatial distribution of tracers and inertial particles in the wake of six islands, considering a randomized release of vortex. From the top to the bottom: (a) ideal tracers; (b),(c) neutrally buoyant particles for St $= 10^{-3}$ and St $= 0.03$, respectively; (d),(e) aerosols for St $= 10^{-3}$ and St $= 0.03$, respectively; (f),(g) bubbles for St $= 10^{-3}$ and St $= 0.03$, respectively. Those snapshots were taken at a time $23.48T_c$ for vortex strength $\omega = 60$ and $\delta_1 = 0$, $\delta_2 = 1.793\,932\,33$, $\delta_3 = 1.358\,841\,53$, $\delta_4 = 1.406\,540\,21$, $\delta_5 = 0.112\,048\,69$, and $\delta_6 = 1.900\,989\,45$.

1. Comparing trajectories of particles with inertia to tracers

Figure 8 shows the distribution of particles in the flow with randomized detachment of the vortices. We observe that the additional mixing introduced by the randomization of the vortex detachment has an impact on the distribution patterns for small Stokes numbers. They become more similar to those of tracers and neutrally buoyant particles. For large Stokes numbers, this mixing effect is not pronounced.

This additional mixing also affects the transition probabilities for particles with small Stokes numbers. They become larger for all types of particles (Fig. 9). Finally, we checked the resulting connectivity maps (Fig. 10). For aerosols, we observe a few more connections due to the increase in mixing, indicating a strong effect on expelling the particles. By contrast, the connectivity map for bubbles with large Stokes number remains unchanged in the number of connections; only the transition probabilities are increased. This can again be explained by the trapping of bubbles in the vortices.

2. Measuring connectivity between islands

Figure 9 presents a transport probability matrix that indicates the likelihood of particles transitioning from one island to another island. This matrix design enables a comparative analysis of particle behavior under randomized vortex conditions, identifying differences in transport dynamics due to particle properties such as inertia and buoyancy. The figure shows a quantified visual representation of how the ran-

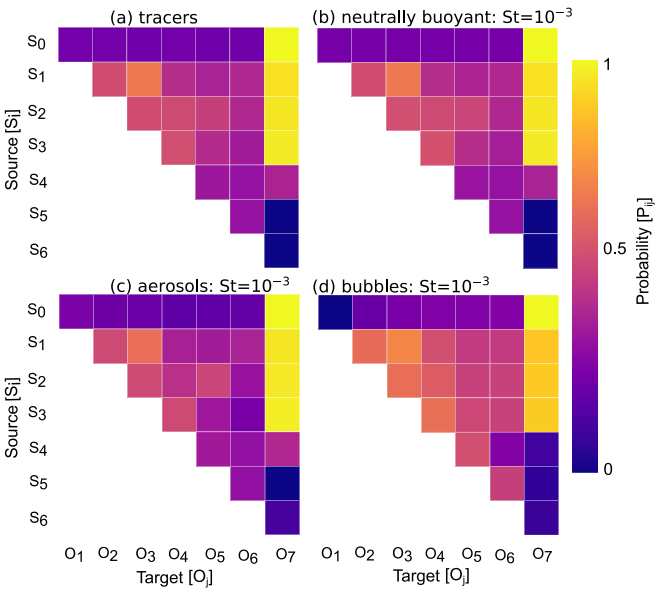

FIG. 9. The transport probabilities for tracers and inertial particles, considering a randomized release of vortex. Geometry: COI. Observation area $[-5, 55]\times[-3, 3]$. (a) Tracers, (b) the neutrally buoyant particles, (c) aerosols, and (d) bubbles. Vortex strength $\omega = 40$ and $\delta_1 = 0$, $\delta_2 = 1.793\,932\,33$, $\delta_3 = 1.358\,841\,53$, $\delta_4 = 1.406\,540\,21$, $\delta_5 = 0.112\,048\,69$, and $\delta_6 = 1.900\,989\,45$.

domized release of vortices affects the dispersal and eventual settling of various particle types, offering insights critical for understanding particle transport phenomena in both natural fluid environments and industrial applications.

In Fig. 10, we illustrate the probability of particle transitions from one island to another under a randomized vortex release timing, highlighting the increased complexity and randomness introduced by the vortex release timing.

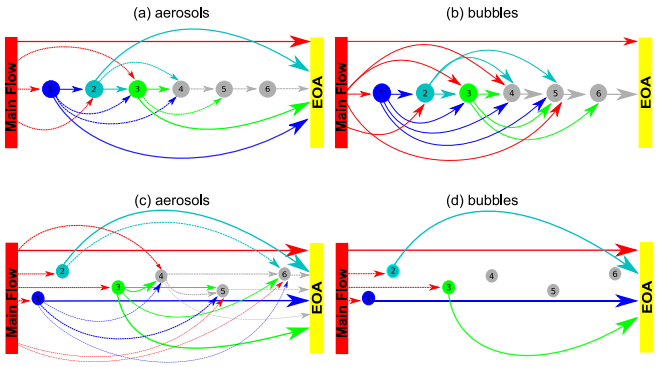

FIG. 10. Connectivity for different geometrical setups for the position of the islands, considering a randomized release of vortex. (a),(b) COI and observation area $[-5, 55]\times[-3, 3]$. (c),(d) RG and observation area $[-5, 45]\times[-5, 5]$. In (a) and (c), we display the connectivity for aerosols. In (b) and (d), we display the connectivity for bubbles. The vortex strengths and the Stokes number are $\omega = 40$ and $\mathrm{St} = 0.03$, respectively, with $\delta_1 = 0$, $\delta_2 = 1.793\,932\,33$, $\delta_3 = 1.358\,841\,53$, $\delta_4 = 1.406\,540\,21$, $\delta_5 = 0.112\,048\,69$, and $\delta_6 = 1.900\,989\,45$.

[1] S. Bialonski, D. A. Caron, J. Schloen, U. Feudel, H. Kantz, and S. D. Moorthi, Phytoplankton dynamics in the Southern California bight indicate a complex mixture of transport and biology, J. Plankton Res. **38**, 1077 (2016).

[2] V. Rossi, E. Ser-Giacomi, C. López, and E. Hernández-García, Hydrodynamic provinces and oceanic connectivity from a transport network help designing marine reserves, Geophys. Res. Lett. **41**, 2883 (2014).

[3] I. Nadal, S. Sammartino, J. García-Lafuente, J. C. Sanchez Garrido, J. Gil-Herrera, M. Hidalgo, and P. Hernández, Hydrodynamic connectivity and dispersal patterns of a transboundary species (*pagellus bogaraveo*) in the Strait of Gibraltar and adjacent basins, Fisher. Oceanogr. **31**, 384 (2022).

[4] P. Monroy, E. Hernández-García, V. Rossi, and C. López, Modeling the dynamical sinking of biogenic particles in oceanic flow, Nonlin. Proc. Geophys. **24**, 293 (2017).

[5] L. Christina and U. Passow, Factors influencing the sinking of POC and the efficiency of the biological carbon pump, Deep Sea Res. Part II: Topic. Stud. Oceanogr. **54**, 639 (2007).

[6] R. Corrado, G. Lacorata, L. Palatella, R. Santoleri, and E. Zambianchi, General characteristics of relative dispersion in the ocean, Sci. Rep. **7**, 46291 (2017).

[7] S. Kelly, E. Popova, Y. Aksenov, R. Marsh, and A. Yool, Lagrangian modeling of arctic ocean circulation pathways: Impact of advection on spread of pollutants, J. Geophys. Res.: Oceans **123**, 2882 (2018).

[8] H. Kumar and R. Rani, Structural and optical characterization of ZNO nanoparticles synthesized by microemulsion route, Intl. Lett. Chem. Phys. Astron. **19**, 26 (2013).

[9] R. G. Henriquez Rivera, X. Zhang, and M. D. Graham, Mechanistic theory of margination and flow-induced segregation in confined multicomponent suspensions: Simple shear and poiseuille flows, Phys. Rev. Fluids **1**, 060501 (2016).

[10] M. U. Babler, L. Biferale, L. Brandt, U. Feudel, K. Guseva, A. S. Lanotte, C. Marchioli, F. Picano, G. Sardina, A. Soldati *et al.*, Numerical simulations of aggregate breakup in bounded and unbounded turbulent flows, J. Fluid Mech. **766**, 104 (2015).

[11] K. Guseva and U. Feudel, Aggregation and fragmentation dynamics in random flows: From tracers to inertial aggregates, Phys. Rev. E **95**, 062604 (2017).

[12] K. Müller, D. A. Fedosov, and G. Gompper, Margination of micro-and nanoparticles in blood flow and its effect on drug delivery, Sci. Rep. **4**, 4871 (2014).

[13] Z. Xu and C. Kleinstreuer, Direct nanodrug delivery for tumor targeting subject to shear-augmented diffusion in blood flow, Medic. Biolog. Eng. Comput. **56**, 1949 (2018).

[14] W. Fornari, A. Formenti, F. Picano, and L. Brandt, The effect of particle density in turbulent channel flow laden with finite size particles in semi-dilute conditions, Phys. Fluids **28**, 033301 (2016).

[15] A. G. Kidanemariam, C. Chan-Braun, T. Doychev, and M. Uhlmann, Direct numerical simulation of horizontal open channel flow with finite-size, heavy particles at low solid volume fraction, New J. Phys. **15**, 025031 (2013).

[16] F. Picano, W.-P. Breugem, and L. Brandt, Turbulent channel flow of dense suspensions of neutrally buoyant spheres, J. Fluid Mech. **764**, 463 (2015).

[17] S. Wood, C. Paris, A. Ridgwell, and E. Hendy, Modelling dispersal and connectivity of broadcast spawning corals at the global scale, Global Ecol. Biogeogr. **23**, 1 (2014).
[18] T. Van der Stocken, D. Carroll, D. Menemenlis, M. Simard, and N. Koedam, Global-scale dispersal and connectivity in mangroves, Proc. Natl. Acad. Sci. **116**, 915 (2019).
[19] T. Van der Stocken, A. K. Wee, D. J. De Ryck, B. Vanschoenwinkel, D. A. Friess, F. Dahdouh-Guebas, M. Simard, N. Koedam, and E. L. Webb, A general framework for propagule dispersal in mangroves, Biolog. Rev. **94**, 1547 (2019).
[20] C. Viatte, C. Clerbaux, C. Maes, P. Daniel, R. Garello, S. Safieddine, and F. Ardhuin, Air pollution and sea pollution seen from space, Surv. Geophys. **41**, 1583 (2020).
[21] D. Siegel, B. Kinlan, B. Gaylord, and S. Gaines, Lagrangian descriptions of marine larval dispersion, Marine Ecol. Prog. Ser. **260**, 83 (2003).
[22] U. Daewel, C. Schrum, and A. Temming, Towards a more complete understanding of the life cycle of brown shrimp (*crangon crangon*): Modelling passive larvae and juvenile transport in combination with physically forced vertical juvenile migration, Fisher. Oceanogr. **20**, 479 (2011).
[23] M. Hufnagl, M. Payne, G. Lacroix, L. J. Bolle, U. Daewel, M. Dickey-Collas, T. Gerkema, M. Huret, F. Janssen, M. Kreus, J. Pätsch, T. Pohlmann, P. Ruardij, C. Schrum, M. D. Skogen, M. C. Tiessen, P. Petitgas, J. K. van Beek, H. W. van der Veer, and U. Callies, Variation that can be expected when using particle tracking models in connectivity studies, J. Sea Res. **127**, 133 (2017).
[24] A. Baudena, E. Ser-Giacomi, I. Jalón-Rojas, F. Galgani, and M. L. Pedrotti, The streaming of plastic in the Mediterranean Sea, Nat. Commun. **13**, 2981 (2022).
[25] F. Chenillat, T. Huck, C. Maes, N. Grima, and B. Blanke, Fate of floating plastic debris released along the coasts in a global ocean model, Mar. Pollut. Bull. **165**, 112116 (2021).
[26] M. Lévy, O. Jahn, S. Dutkiewicz, M. J. Follows, and F. d'Ovidio, The dynamical landscape of marine phytoplankton diversity, J. R. Soc. Interface **12**, 20150481 (2015).
[27] A. Daitche and T. Tél, Memory effects in chaotic advection of inertial particles, New J. Phys. **16**, 073008 (2014).
[28] T. Wang, S. Zhao, L. Zhu, J. C. McWilliams, L. Galgani, R. M. Amin, R. Nakajima, W. Jiang, and M. Chen, Accumulation, transformation and transport of microplastics in estuarine fronts, Nat. Rev. Earth Environ. **3**, 795 (2022).
[29] I. S. Abihssira-García, T. Kögel, A. Gomiero, T. Kristensen, M. Krogstad, and P. A. Olsvik, Distinct polymer-dependent sorption of persistent pollutants associated with atlantic salmon farming to microplastics, Mar. Pollut. Bull. **180**, 113794 (2022).
[30] K. L. Law, S. Morét-Ferguson, N. A. Maximenko, G. Proskurowski, E. E. Peacock, J. Hafner, and C. M. Reddy, Plastic accumulation in the North Atlantic subtropical gyre, Science **329**, 1185 (2010).
[31] S. Liubartseva, G. Coppini, R. Lecci, and E. Clementi, Tracking plastics in the Mediterranean: 2D Lagrangian model, Mar. Pollut. Bull. **129**, 151 (2018).
[32] Á. M. Felicísimo, J. Muñoz, and J. González-Solis, Ocean surface winds drive dynamics of transoceanic aerial movements, PLoS One **3**, e2928 (2008).
[33] C. B. Paris, L. M. Chérubin, and R. K. Cowen, Surfing, spinning, or diving from reef to reef: Effects on population connectivity, Marine Ecol. Prog. Ser. **347**, 285 (2007).
[34] L.-M. Lebreton, S. Greer, and J. C. Borrero, Numerical modelling of floating debris in the world's oceans, Mar. Pollut. Bull. **64**, 653 (2012).
[35] C. B. Paris, J. Atema, J.-O. Irisson, M. Kingsford, G. Gerlach, and C. M. Guigand, Reef odor: A wake up call for navigation in reef fish larvae, PloS One **8**, e72808 (2013).
[36] E. Van Sebille, S. M. Griffies, R. Abernathey, T. P. Adams, P. Berloff, A. Biastoch, B. Blanke, E. P. Chassignet, Y. Cheng, C. J. Cotter *et al.*, Lagrangian ocean analysis: Fundamentals and practices, Ocean Model. **121**, 49 (2018).
[37] R. K. Cowen, K. M. Lwiza, S. Sponaugle, C. B. Paris, and D. B. Olson, Connectivity of marine populations: Open or closed? Science **287**, 857 (2000).
[38] J. Nishikawa, S. Nishida, M. Moku, K. Hidaka, and K. Kawaguchi, Biomass, abundance, and vertical distribution of micronekton and large gelatinous zooplankton in the Subarctic Pacific and the Bering Sea during the summer of 1997, J. Oceanogr. **57**, 361 (2001).
[39] R. D. Vilela and A. E. Motter, Can aerosols be trapped in open flows? Phys. Rev. Lett. **99**, 264101 (2007).
[40] M. Sandulescu, E. Hernández-García, C. López, and U. Feudel, Kinematic studies of transport across an island wake, with application to the canary islands, Tellus A: Dynam. Meteorol. Oceanogr. **58**, 605 (2006).
[41] J. C. Zahnow, R. D. Vilela, U. Feudel, and T. Tél, Aggregation and fragmentation dynamics of inertial particles in chaotic flows, Phys. Rev. E **77**, 055301(R) (2008).
[42] R. de la Fuente, G. Drótos, E. Hernández-García, and C. López, Network and geometric characterization of three-dimensional fluid transport between two layers, Phys. Rev. E **104**, 065111 (2021).
[43] M. R. Maxey and J. J. Riley, Equation of motion for a small rigid sphere in a nonuniform flow, Phys. Fluids **26**, 883 (1983).
[44] R. Gatignol *et al.*, The Faxèn formulae for a rigid particle in an unsteady non-uniform Stokes flow, J. Méc. Théor. Appl. **1**, 143 (1983).
[45] T. Auton, J. Hunt, and M. Prud'Homme, The force exerted on a body in inviscid unsteady nonuniform rotational flow, J. Fluid Mech. **197**, 241 (1988).
[46] I. J. Benczik, Z. Toroczkai, and T. Tél, Selective sensitivity of open chaotic flows on inertial tracer advection: Catching particles with a stick, Phys. Rev. Lett. **89**, 164501 (2002).
[47] E. Calzavarini, M. Cencini, D. Lohse, F. Toschi *et al.*, Quantifying turbulence-induced segregation of inertial particles, Phys. Rev. Lett. **101**, 084504 (2008).
[48] J. Bec, A. Celani, M. Cencini, and S. Musacchio, Clustering and collisions of heavy particles in random smooth flows, Phys. Fluids **17**, 073301 (2005).
[49] L. Fiabane, R. Zimmermann, R. Volk, J.-F. Pinton, and M. Bourgoin, Clustering of finite-size particles in turbulence, Phys. Rev. E **86**, 035301(R) (2012).
[50] M. Gibert, H. Xu, and E. Bodenschatz, Where do small, weakly inertial particles go in a turbulent flow? J. Fluid Mech. **698**, 160 (2012).
[51] K. Guseva, U. Feudel, and T. Tél, Influence of the history force on inertial particle advection: Gravitational effects and horizontal diffusion, Phys. Rev. E **88**, 042909 (2013).

[52] M. Maxey, The motion of small spherical particles in a cellular flow field, Phys. Fluids **30**, 1915 (1987).

[53] L.-P. Wang and M. R. Maxey, Settling velocity and concentration distribution of heavy particles in homogeneous isotropic turbulence, J. Fluid Mech. **256**, 27 (1993).

[54] K. Guseva, A. Daitche, U. Feudel, and T. Tél, History effects in the sedimentation of light aerosols in turbulence: The case of marine snow, Phys. Rev. Fluids **1**, 074203 (2016).

[55] C. Jung, T. Tél, and E. Ziemniak, Application of scattering chaos to particle transport in a hydrodynamical flow, Chaos: Interdiscipl. J. Nonlin. Sci. **3**, 555 (1993).

[56] I. J. Benczik, Z. Toroczkai, and T. Tél, Advection of finite-size particles in open flows, Phys. Rev. E **67**, 036303 (2003).

[57] J. C. Zahnow, R. D. Vilela, U. Feudel, and T. Tél, Coagulation and fragmentation dynamics of inertial particles, Phys. Rev. E **80**, 026311 (2009).

[58] R. Reigada, F. Sagués, and J. M. Sancho, Inertial effects on reactive particles advected by turbulence, Phys. Rev. E **64**, 026307 (2001).

[59] E. Michaelides, *Particles, Bubbles & Drops: Their Motion, Heat and Mass Transfer* (World Scientific, Singapore, 2006).

[60] M. A. Sanjuan, J. Kennedy, C. Grebogi, and J. A. Yorke, Indecomposable continua in dynamical systems with noise: Fluid flow past an array of cylinders, Chaos: Interdiscipl. J. Nonlin. Sci. **7**, 125 (1997).